



Electrocatalysis Hot Paper



Electrochemical Phase Evolution of Metal-Based Pre-Catalysts for High-Rate Polysulfide Conversion

Meng Zhao⁺, Hong-Jie Peng⁺, Bo-Quan Li, Xiao Chen, Jin Xie, Xinyan Liu, Qiang Zhang, and Jia-Qi Huang*

Abstract: *In situ* evolution of electrocatalysts is of paramount importance in defining catalytic reactions. Catalysts for aprotic electrochemistry such as lithium–sulfur (Li-S) batteries are the cornerstone to enhance intrinsically sluggish reaction kinetics but the true active phases are often controversial. Herein, we reveal the electrochemical phase evolution of metal-based pre-catalysts (Co₄N) in working Li-S batteries that renders highly active electrocatalysts (CoS_x). Electrochemical cycling induces the transformation from single-crystalline Co₄N to polycrystalline CoS_x that are rich in active sites. This transformation propels all-phase polysulfide-involving reactions. Consequently, Co₄N enables stable operation of high-rate (10 C, 16.7 mA cm⁻²) and electrolyte-starved (4.7 μL mg⁻¹) Li-S batteries. The general concept of electrochemically induced sulfurization is verified by thermodynamic energetics for most of low-valence metal compounds.

Introduction

Phase and structural evolution of a working catalyst play an essential role in governing the catalytic activity and reaction kinetics.^[1,2] For instance, dissolved cobalt phosphate was transformed under oxidizing potential into a solid catalyst for water oxidation.^[3] Transition-metal chalcogenides and pnictides are also known as water oxidation pre-catalysts with a surface oxidized layer as the true active phase.^[4–6] Nevertheless, the understanding of *in situ* catalyst evolution is currently limited to reactions occurring at solid/gas interfaces^[2] or in protic (aqueous) conditions,^[3–5] leaving aprotic reactions as an empty field. The aprotic electrochemical reactions is the cornerstone of alkali metal (Li/Na/K)-

chalcogen (S/O₂) batteries with overwhelming advantages in energy density.^[7,8] These batteries unfortunately suffer from multi-electron transferring that normally induces reaction complexity and sluggish kinetics in a working device.^[9]

Introducing mobile or solid catalysts have recently validated to resolve the above issues.^[10–12] However, it is unclear at the moment how these catalysts evolve in an aprotic environment and how such evolution defines the catalytic behaviors. The role of large-radius alkali metal cations (vs. hydronium) and intermediates/reactants beyond H₂O/OH⁻ (for example, lithium polysulfides in Li-S batteries) present in the aprotic environment needs to be unveiled to understand the electrochemical phase evolution of an electrocatalyst and identify the true active catalytic phases/sites. This understanding should be a prerequisite for rational design of new catalysts and better batteries.

Herein, we report the electrochemical phase evolution of metal-based pre-catalysts in working Li-S batteries, rendering mosaic-like, bulk-sulfurized catalysts that are highly adaptive to the polysulfide-rich aprotic environment and highly active for propelling the kinetics of all-phase polysulfide-involving reactions at high current rates (Figure 1 A). Co₄N serves as an exemplified pre-catalyst.^[13] High-resolution transmission electron microscopy (HRTEM) observation unveils the mosaicking of 30–50 nm pristine Co₄N particles into phase-bounded 2–10 nm particles after electrochemical cycling. The resultant mosaic-like catalysts not only consist of pristine Co₄N phase but also various sulfurized phases of CoS_x (9/8 < *x* < 2) that are catalytically active.^[14] As evidenced by microscopic and spectroscopic observations, the *in situ* mosaicking process proceeds through etching of low-valence metal atoms by polysulfides. This etching mechanism is found to be universal for most of transition metals according to theoretical calculations. With significantly increased number of active interfaces and CoS_x phases, electrochemically cycled Co₄N possesses more superior catalytic activities for catalyzing polysulfide conversion than pristine Co₄N (by 7.6–58% regarding the critical kinetics parameters). High-rate and electrolyte-starved Li-S batteries are thus enabled owing to the capability of Co₄N evolved *in situ* to reduce the cell polarization significantly (by up to 55%).

Results and Discussion

Monodispersed Co₄N nanoparticles on conductive nitrogen-doped graphene substrates (Co₄N/NG), as well as bulk Co₄N, were synthesized (Supporting Information, Figures S1–

[*] M. Zhao,^[†] B. Q. Li, Prof. J.-Q. Huang
School of Materials Science & Engineering
Beijing Institute of Technology, Beijing 100081 (P. R. China)
and
Advanced Research Institute of Multidisciplinary Science
Beijing Institute of Technology, Beijing 100081 (P. R. China)
E-mail: jqhuang@bit.edu.cn

Dr. H.-J. Peng,^[†] Dr. X. Chen, J. Xie, Dr. X. Liu, Prof. Q. Zhang
Department of Chemical Engineering, Tsinghua University
Beijing 100084 (P. R. China)

Dr. H.-J. Peng,^[†] B. Q. Li, Dr. X. Liu
Department of Chemical Engineering, Stanford University
Stanford, CA 94305 (USA)

[†] These authors contributed equally to this work.

Supporting information and the ORCID identification number(s) for the author(s) of this article can be found under:
<https://doi.org/10.1002/anie.202003136>.

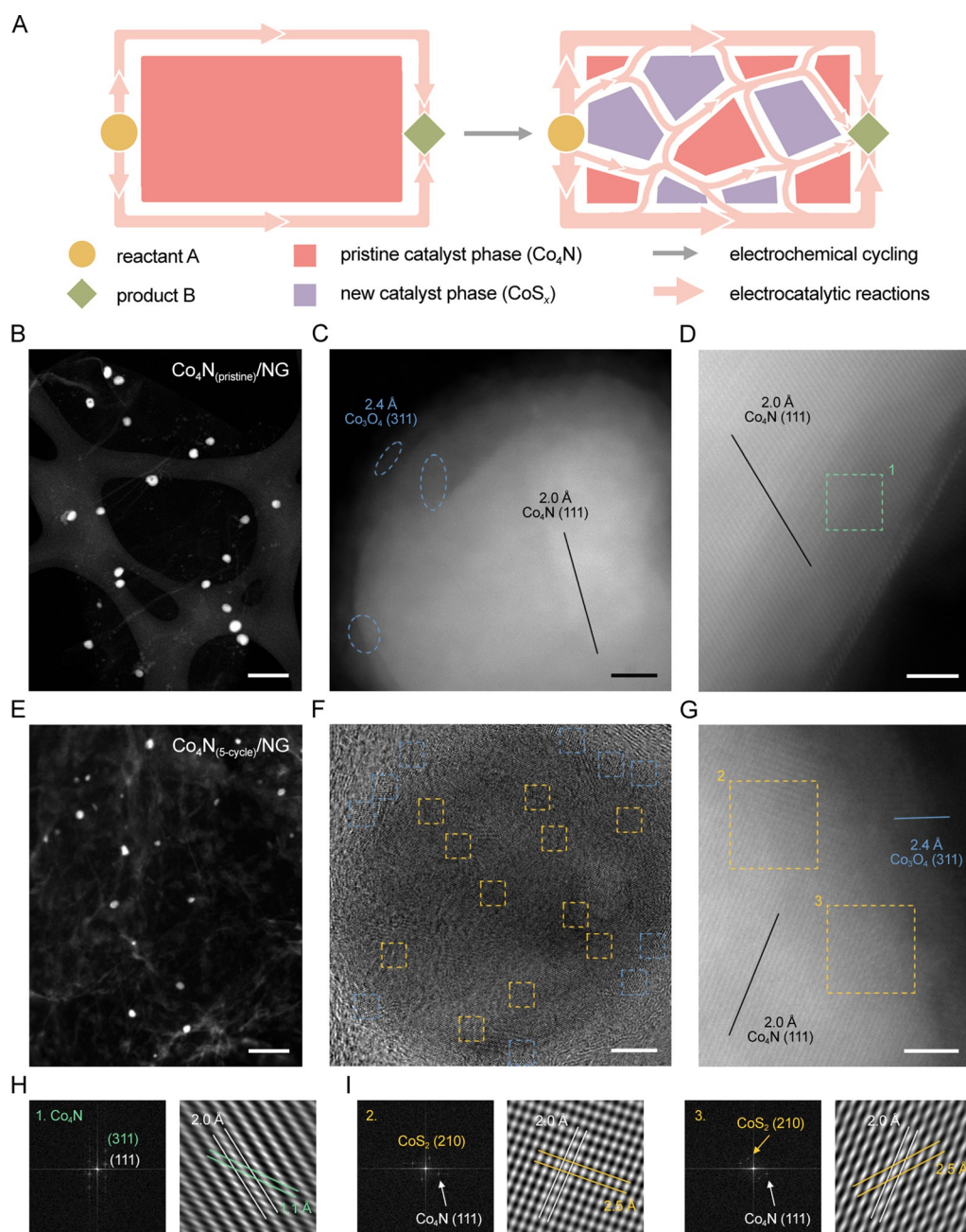


Figure 1. A) Representation of metal-rich compounds as pre-catalysts (herein exemplified as Co_4N) undergo in situ mosaicking phase evolution in working batteries. B)–I) High-angle annular dark-field scanning transmission electron microscopy (HAADF-STEM) images of B)–D) $\text{Co}_4\text{N}_{(\text{pristine})}/\text{NG}$, E), G) $\text{Co}_4\text{N}_{(5\text{-cycle})}/\text{NG}$, and F) the HRTEM image of $\text{Co}_4\text{N}_{(5\text{-cycle})}/\text{NG}$. $\text{Co}_4\text{N}_{(5\text{-cycle})}/\text{NG}$ was at the fully charged state. Scale bars: B), E) 200 nm, C), F) 5 nm, D), G) 2 nm. Fast Fourier transform (FFT) patterns and corresponding inverse FFT images of the selected square regions marked in H) (D) and I) (G).

S5). The hybridization with Co_4N did not sacrifice the surface area of graphene much (Supporting Information, Figure S6). The high surface area benefits the precipitation of insulating solids (S/Li₂S).^[14] The pristine Co_4N (denoted as $\text{Co}_4\text{N}_{(\text{pristine})}/\text{NG}$) exhibits as 30–50 nm monodispersed particles (Figure 1B). Each particle is in single-crystalline cubic Co_4N phase decorated with polycrystalline surface oxides such as Co_3O_4 (Figure 1C, D, and H). The surface oxidation is unavoidable due to the vulnerable nature of metal-rich compounds.^[4] After five cycles in Li-S batteries, the mono-

dispersity of Co_4N on graphene (denoted as $\text{Co}_4\text{N}_{(5\text{-cycle})}/\text{NG}$) was well-retained (Figure 1E). However, the bulk Co_4N phase turned into an assembly of interconnected 2–10 nm particles (Figure 1F). Besides the pristine oxide particles, cobalt sulfide particles such as CoS_2 are observed in $\text{Co}_4\text{N}_{(5\text{-cycle})}$ (Figure 1G,I). Other sulfurized phases such as amorphous CoS_x , as well as abundant phase boundaries, are also indexed with rigorous crystallographic analysis (Supporting Information, Figure S7–S11). Note that these CoS_x particles not only appear near the surface of $\text{Co}_4\text{N}_{(5\text{-cycle})}$ but also within

the central region, implying deep penetration of sulfur and mosaicking of the whole particle (Supporting Information, Figures S8 and S9).

The origin of phase evolution is revealed through multiple characterization methods. Unlike graphene, bulk Co_4N particles exhibit a remarkable ability to decolorize the Li_2S_4 solution, implying the strong interactions between Co_4N and polysulfides (Supporting Information, Figure S12). HAADF-STEM elemental mapping of a single $\text{Co}_4\text{N}_{(\text{pristine})}$ particle reveals its core/shell structure (Figure 2A). The thickness of oxidized shell is 2–3 nm. Electrochemical cycling renders $\text{Co}_4\text{N}_{(\text{S-cycle})}$ significant sulfur signals (Figure 2B). Sulfur is dispersed across the whole particle, differing from surface enriched oxygen. This result confirms the observation of bulk sulfurization (Supporting Information, Figures S8–S11). In contrast, polysulfide-treated but uncycled Co_4N (denoted as $\text{Co}_4\text{N}_{(\text{ads})}$) is only featured with surface sulfurized layer, indicating the profound influence of electrochemical cycling on sulfurization (Figure 2C). The sulfurization is further validated by X-ray photoelectron spectroscopy (XPS) (Figure 2D,E). $\text{Co}_4\text{N-Li}_2\text{S}_4$ exhibits predominant Co–S bond formation with metallic Co in Co_4N and Li–S/S–S bonds in Li_2S_4 disappearing. The comparison between S 2p spectra of cycled graphene and $\text{Co}_4\text{N/NG}$ further confirms the formation of Co–S in working batteries (Supporting Information, Figure S13). It is therefore reasonably deduced that low-valence Co in Co_4N is initially subjected to the polysulfide etching and the as-generated atomic Co–S species then evolve into interconnected CoS_x particles.

To verify above polysulfide-etching induced phase evolution mechanism, we conducted density functional theory (DFT) calculation in various aspects. The formation of multiple Co vacancies in the Co_4N (111) surface is modeled (Figure 3A). The exothermic reaction between etched Co

atom and high-order polysulfides (exemplified as the nominal reaction $\text{Li}_2\text{S}_8 + \text{Co} \rightarrow \text{Li}_2\text{S}_6 + \text{CoS}_2$ (bulk)) enables the endothermic vacancy formation process. Figure 3B shows the energetics of single vacancy (SV), double vacancy (DV), and triple vacancy (TV) formation assisted by polysulfide etching. The energetically most favorable pathway (bold black in Figure 3B) shows the preference of N-uncoordinated surface Co atom (atom i shown in Figure 3A) being etched over N-coordinated Co atoms (ii and iii) and N-uncoordinated subsurface Co atom (iv). This observation is in good accordance with the XPS results that low-valence Co in Co_4N is etched to form corresponding sulfides. Also the comparison between states 6 and 7 in Figure 3A, B shows the etching of subsurface Co (iv) prior to complete etching of surface Co (ii after iii), offering an energetic insight into why sulfur penetrates into the central region of Co_4N during phase evolution.

The polysulfide-etching induced phase evolution mechanism is further investigated in a broad range of Co-based compounds (CoB , Co_2C , CoN , Co_3O_4 , Co_2P , CoP , CoS_2 , and CoSe_2). Some of these compounds have been demonstrated as efficient catalysts for polysulfide redox reactions.^[12,14,15] The formation energies of Co SV ($\Delta E_{\text{form}}^{\text{SV}}$) serves as an energetic

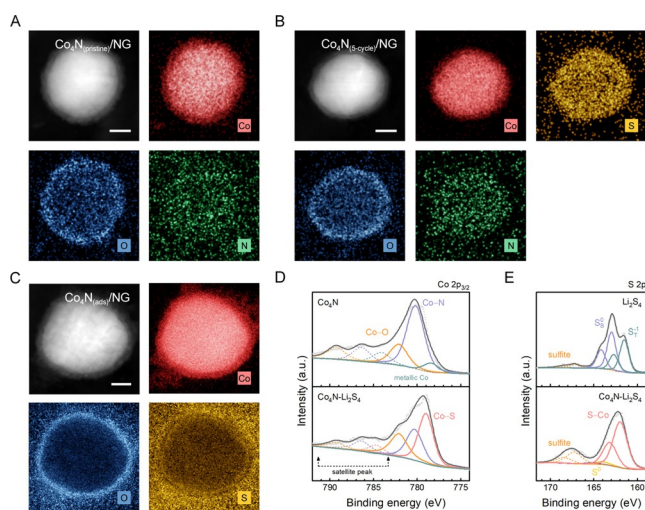


Figure 2. Characterization of electrochemical phase evolution. A)–C) HAADF-STEM images and corresponding elemental mapping of A) $\text{Co}_4\text{N}_{(\text{pristine})}/\text{NG}$, B) $\text{Co}_4\text{N}_{(\text{S-cycle})}/\text{NG}$, and C) $\text{Co}_4\text{N}_{(\text{ads})}/\text{NG}$. Scale bars: 10 nm. D), E) XPS fine spectra, including D) Co $2p_{3/2}$ spectra of bulk Co_4N before and after Li_2S_4 adsorption ($\text{Co}_4\text{N-Li}_2\text{S}_4$) and E) S 2p spectra of pristine Li_2S_4 and $\text{Co}_4\text{N-Li}_2\text{S}_4$. Detailed assignment of XPS peaks are shown in the Supporting Information, Table S1.

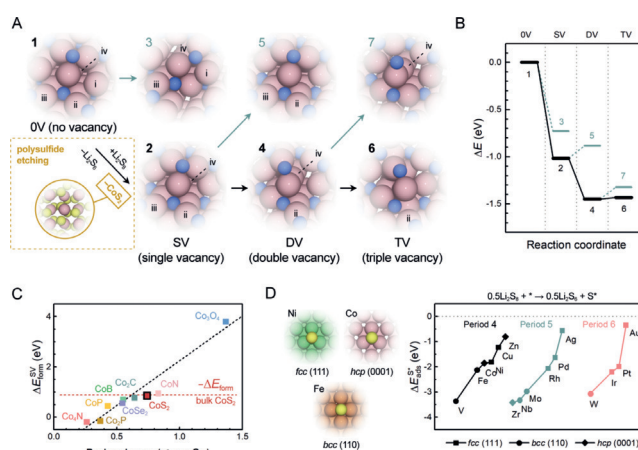


Figure 3. Theoretical investigation of electrochemical phase evolution. A) Illustration of polysulfide-etching induced phase evolution, showing optimized atomic configurations of Co_4N (111) surfaces with zero Co vacancy (0 V), SV, DV, and TV. The Co vacancy formation is enabled by the exothermic reaction $\text{Li}_2\text{S}_8 + \text{Co} \rightarrow \text{Li}_2\text{S}_6 + \text{CoS}_2$ (bulk) as each arrow represented. Uncoordinated Co atoms and Co atoms coordinated with N are marked as (i, iv) and (ii, iii), respectively. N-uncoordinated Co atoms i and iv are present in the surface and subsurface layer, respectively. Co pink, N blue, S yellow spheres. B) Energetics diagrams of the Co-vacancy formation processes shown in (A). The indices of each states correspond to those in (A). The energetically most favorable pathway is marked as bold black. C) $\Delta E_{\text{form}}^{\text{SV}}$ in various Co-based compounds as a function of q of Co atoms in each bulk compound. The black dashed line shows the quasi-linear relationship between $\Delta E_{\text{form}}^{\text{SV}}$ and q . The red dashed line represents the formation energy ($-\Delta E_{\text{form}}$) of bulk CoS_2 through reaction $\text{Li}_2\text{S}_8 + \text{Co} \rightarrow \text{Li}_2\text{S}_6 + \text{CoS}_2$ (bulk). D) Adsorption energies of S^* ($\Delta E_{\text{ads}}^{\text{S}^*}$) on various metal surfaces as a function of atomic numbers, along with the representative optimized binding configurations of S^* on surfaces of fcc (111), bcc (110), and hcp (0001). Ni green, Co pink, Fe orange, S yellow spheres. The S^* is produced through reaction $0.5\text{Li}_2\text{S}_8 + * \rightarrow 0.5\text{Li}_2\text{S}_6 + \text{S}^*$ (asterisk represents the surface site).

indicator (with optimized structures shown in the Supporting Information, Figure S14) to compare with the formation energy of bulk CoS_2 through reaction $\text{Li}_2\text{S}_8 + \text{Co} \rightarrow \text{Li}_2\text{S}_6 + \text{CoS}_2$ (bulk) and validate the possibility of phase evolution of these compounds in a polysulfide-enriched environment. Figure 3C clearly shows the quasi-linear correlation between $\Delta E_{\text{form}}^{\text{SV}}$ and the average Bader charge (q) of Co atoms in each bulk compound. And compounds with q lower than that of CoS_2 (0.74) have lower $\Delta E_{\text{form}}^{\text{SV}}$ than $-\Delta E_{\text{form}}$ of bulk CoS_2 and therefore should be subjected to a phase transition to sulfides with the presence of polysulfides. This finding points out the fact that in situ generated CoS_x might be the true active phases accounting for catalytic activity observed for above Co-based compounds with low-valence Co atoms.

The affinity between low-valence metal atoms and S in high-order polysulfides could be further extended to other metals and measured by the adsorption energies of atomic S (S^*) on metal surfaces (Figure 3D). These metals include simple *fcc*, *bcc*, and *hcp* metals that are widely investigated in heterogeneous catalysis and surface science,^[16] and the most inert flat surface, that is, (111) for *fcc*, (110) for *bcc* and (0001) for *hcp* metals, is modeled. It is shown that on all metals, from strong-binding early transition metals V, Zr, Nb, Mo, and W to weak-binding coinage metals Ag and Au, the adsorption of S^* , which is produced from the fragmentation of Li_2S_8 to Li_2S_6 , is exothermic. Actually, extensive previous studies have evidenced the formation of low valence metal-S bond on different metal-rich compounds.^[17,18] Therefore, from a theoretical perspective, we conclude that most of metals and very likely their metal-rich alloys and compounds containing zero-valence metal atoms will be either completely or partially sulfurized when employed in Li-S batteries. Probing the true catalytic phases is then crucial.

It is then important to validate the effect of electrochemical mosaicking phase evolution on catalytic activities. All polysulfide-involving reactions in aprotic Li-S batteries are categorized by phases and their kinetics were studied using different methods (see the Experimental Section).^[19] Also, to unveil the role of various components present in the (pre)-catalysts before and after electrochemical cycling, hybrid materials consisting of NG and Co_3O_4 , Co_9S_8 , and CoS_2 were synthesized and evaluated (Supporting Information, Figures S15–S17).

For liquid–liquid polysulfide interconversion that was probed in Li_2S_6 | Li_2S_6 symmetric cells, $\text{Co}_4\text{N}_{(5\text{-cycle})}/\text{NG}$ renders 58% and 119% enhancement (compared to $\text{Co}_4\text{N}_{(\text{pristine})}/\text{NG}$) in maximum response current and total transferred charge, respectively (Figure 4A; Supporting Information, Figure S18A). Concurrently, the charge-transfer impedance of $\text{Co}_4\text{N}_{(5\text{-cycle})}/\text{NG}$ is 51% smaller than $\text{Co}_4\text{N}_{(\text{pristine})}/\text{NG}$ (Supporting Information, Figure S19A).

For liquid–solid Li_2S deposition that was investigated by chronoamperometry of Li | Li_2S_8 cells, both $\text{Co}_4\text{N}_{(\text{pristine})}/\text{NG}$ and $\text{Co}_4\text{N}_{(5\text{-cycle})}/\text{NG}$ exhibit a distinctly predominant potentiostatic current peak in against the NG substrates (Figure 4B), corresponding to the point at which the Li_2S /electrolyte/catalyst triple-phase boundary reaches its maximum length.^[20] Nevertheless, $\text{Co}_4\text{N}_{(5\text{-cycle})}/\text{NG}$ possesses the earliest peak position (ca. 7.6% and 36% earlier than

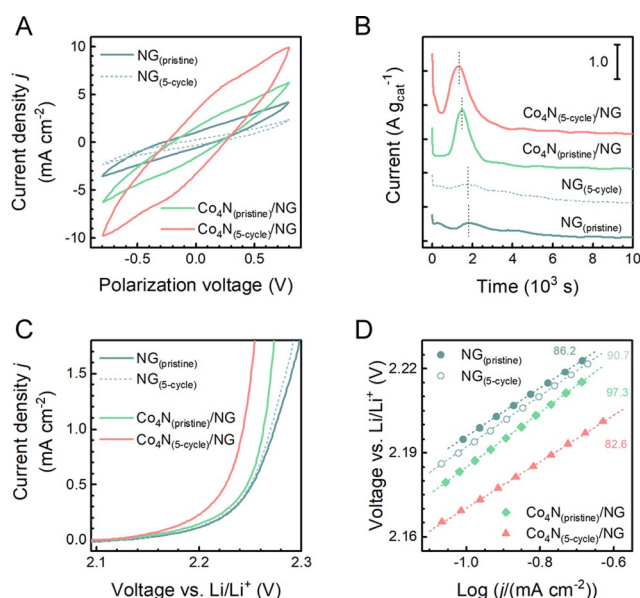


Figure 4. The effect of electrochemical phase evolution on catalytic performance toward various polysulfide-involving reactions. Four types of electrode, $\text{NG}_{(\text{pristine})}$, $\text{NG}_{(5\text{-cycle})}$, $\text{Co}_4\text{N}_{(\text{pristine})}/\text{NG}$, and $\text{Co}_4\text{N}_{(5\text{-cycle})}/\text{NG}$, served as working electrodes. A) Cyclic voltammetry (CV) curves of Li_2S_6 | Li_2S_6 symmetric cells, showing the kinetics of liquid–liquid polysulfide interconversion. B) Chronoamperometry curves of Li | Li_2S_8 cells, showing the kinetics of liquid–solid Li_2S deposition. C) Linear sweep voltammetry (LSV) curves (anodic scan of CV shown in the Supporting Information, Figure S20) of Li | S cells and D) corresponding Tafel plots, showing the kinetics of solid–liquid Li_2S oxidation.

$\text{Co}_4\text{N}_{(\text{pristine})}/\text{NG}$ and NG), demonstrating the highest Li_2S nucleation/growth rate.

For solid–liquid Li_2S oxidation that was studied by LSV of Li | S cells, $\text{Co}_4\text{N}_{(5\text{-cycle})}/\text{NG}$ reduces the overpotential by about 20 mV (at 1.0 mA cm^{-2}) from $\text{Co}_4\text{N}_{(\text{pristine})}/\text{NG}$ and decreases the Tafel slope from 97.3 mV dec^{-1} ($\text{Co}_4\text{N}_{(\text{pristine})}/\text{NG}$) to 82.6 mV dec^{-1} (Figure 4C,D). In contrast, $\text{NG}_{(\text{pristine})}$ and $\text{NG}_{(5\text{-cycle})}$ exhibit little change in Li_2S oxidation kinetics.

To further elucidate the importance of electrochemical cycling, the liquid–liquid kinetics with other control samples including $\text{Co}_4\text{N}_{(\text{ads})}/\text{NG}$, $\text{Co}_3\text{O}_4/\text{NG}$, $\text{Co}_9\text{S}_8/\text{NG}$, and CoS_2/NG were probed (Supporting Information, Figures S18B–D and 19B–E). All these samples exhibit neither the comparable catalytic activity to $\text{Co}_4\text{N}/\text{NG}$ or as-profound effect of electrochemical cycling on the redox current and the impedance. Since the theoretical analysis reveals that only Co_4N is inclined to phase evolution among these Co-based compounds, the profound enhancement for all polysulfide-involving reactions can only be ascribed to the electrochemical phase evolution.

To fully exert its merits, the $\text{Co}_4\text{N}/\text{NG}$ pre-catalyst was employed as a functional membrane on routine polypropylene (PP) separator (Supporting Information, Figure S21).^[8] Owing to the superior catalytic activity in situ attained in a working Li-S battery, $\text{Co}_4\text{N}/\text{NG}$ results in remarkable rate performance especially when current density exceeds 0.5 C (1.0 C = 1672 mA g_s^{-1} ; Figure 5A). In particular, average capacities at 4 and 10 C are 836 and 760 mAh g_s^{-1} (194% and 396% higher than NG), respectively. Such a superb rate

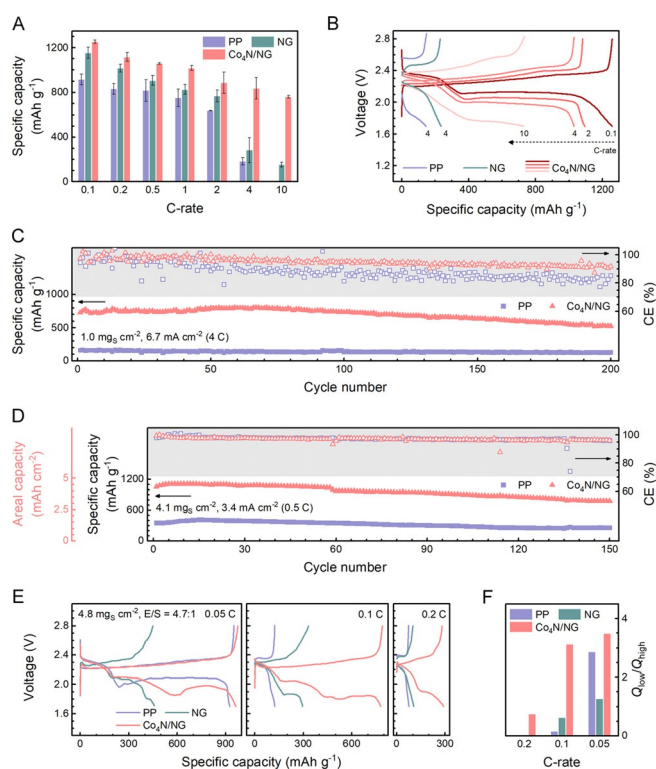


Figure 5. $\text{Co}_4\text{N}/\text{NG}$ pre-catalysts for high-rate and electrolyte-starved Li-S batteries. High-rate Li-S batteries: A) rate performance showing capacities in average and with error bars; B) galvanostatic discharge-charge profiles at various current densities; C) cycling performance at a high current density of 4.0 C (6.7 mA cm^{-2}); D) cycling performance at 0.5 C (3.4 mA cm^{-2}) with high-loading sulfur cathodes. Electrolyte-starved Li-S batteries: E) galvanostatic discharge-charge profiles and F) $Q_{\text{low}}/Q_{\text{high}}$ ratios at various current densities. Areal sulfur loadings (unit: $\text{mg}_\text{s} \text{ cm}^{-2}$): A)–C) 1.0, D) 4.1, E), F) 4.8. Electrolyte-to-sulfur (E/S) ratios ($\mu\text{L mg}_\text{s}^{-1}$): A)–C) 19, D) 12, E), F) 4.7.

capability also expresses as small voltage polarization with which $\text{Co}_4\text{N}/\text{NG}$ cells sustain the sluggish Li_2S deposition (featured as low-voltage plateau) at rates of $>2 \text{ C}$ (3.4 mA cm^{-2}); whereas controlled PP and NG cells lose the above feature owing to the large overpotential, thereby delivering low capacity (Figure 5B; Supporting Information, Figure S22). The difference in rate performance agrees well with the kinetics investigation (Figure 4) and electrochemical impedances (Supporting Information, Figure S23).

Besides the rate capability, Co_4N also endows the Li-S cell with a strong ability to withstand polysulfide shuttle via rapid transformation of mobile polysulfides into immobile phases.^[11] As a result, $\text{Co}_4\text{N}/\text{NG}$ cells exhibit greatly improved cycling stability in terms of both capacity and Coulombic efficiency (CE; Supporting Information, Figures S24, S25). Detailed overpotential analysis further suggests smooth phase-transferring (that is, Li_2S deposition/oxidation) reactions in $\text{Co}_4\text{N}/\text{NG}$ cell, in contrast to the high overpotential in PP cells and kinetics degradation in NG cells (Supporting Information, Figure S26). This trend in capacity fading is also validated by morphological differences in cycled cathode: large solid (S/ Li_2S) precipitates are observed without Co_4N ; while the solid deposition is uniform with Co_4N and the

porous electrode architecture is well-preserved (Supporting Information, Figure S27). Co_4N also results in clean and polysulfide-uncontaminated separators and compact anode with uniform lithium plating/stripping, indicating that kinetics regulation offered by Co_4N ameliorates the damage from shuttle to the battery (Supporting Information, Figures S28, S29).

Owing to the dual effect of Co_4N on improving rate and cycling performance, Co_4N enables stable cell cycling at a high rate of 4 C (6.7 mA cm^{-2}) with a cyclic capacity decay rate of 0.17% (with respect to the maximum capacity) and average CE of 95.3% for 200 cycles; while the average capacity and CE of PP cell are only $138 \text{ mAh g}_\text{s}^{-1}$ and 88.6%, manifesting much inferior high-rate cyclability (Figure 5C). $Q_{\text{low}}/Q_{\text{high}}$, the capacity ratio of low/high voltage plateaus as a key descriptor of polysulfide-to- Li_2S conversion efficiency,^[21] trends to increase with cycling for $\text{Co}_4\text{N}/\text{NG}$ cells; whereas for PP and NG cells, $Q_{\text{low}}/Q_{\text{high}}$ tends to decrease (Supporting Information, Figure S30). The change in $Q_{\text{low}}/Q_{\text{high}}$ of $\text{Co}_4\text{N}/\text{NG}$ cells is in accordance with the activation of Co_4N pre-catalyst.

High-rate performance enabled by Co_4N was also achieved on high-sulfur-loading cells ($4.1 \text{ mg}_\text{s} \text{ cm}^{-2}$). The advantages of Co_4N in improving sulfur utilization and stabilizing electrochemical interfaces (indicated by CE) are further elucidated (Figure 5D; Supporting Information, Figure S31). At 0.5 C (3.4 mA cm^{-2}), the $\text{Co}_4\text{N}/\text{NG}$ cell delivered a maximum capacity of $1109 \text{ mAh g}_\text{s}^{-1}$ (4.5 mAh cm^{-2}) and maintained $>70\%$ after 150 cycles, which is 204% higher than that retained in a PP cell. Note that such remarkable performance is attained on a routine unmodified carbon/sulfur cathode with tiny addition of Co_4N (ca. 1.0% and 13% by weight of Co_4N and $\text{Co}_4\text{N}/\text{NG}$, respectively). This further demonstrates the superb catalytic ability of Co_4N -derived compounds.

As one of the current directions for aprotic Li-S batteries is to reduce the E/S ratio toward high device energy density,^[22] the even sluggish reaction kinetics under electrolyte-starved conditions remain a huge challenge. At a low E/S ratio of $4.7 \mu\text{L mg}_\text{s}^{-1}$, the controlled PP cell possesses a typical two-plateau discharge profile but large initial low-plateau overpotential at 0.05 C, which becomes unsurmountable at 0.1 and 0.2 C and thus impedes the conversion to Li_2S (Figure 5E). In contrast, $\text{Co}_4\text{N}/\text{NG}$ retains the low discharge plateau at each rate. Interestingly, the NG cell possesses much lower capacity than PP at 0.05 C but basically maintains two discharge plateaus at 0.1 and 0.2 C. That is explained by extra electrolyte required to wet NG or $\text{Co}_4\text{N}/\text{NG}$ membrane, in turn lifting the low threshold of electrolyte amount for NG and $\text{Co}_4\text{N}/\text{NG}$ cells. Despite that, NG and $\text{Co}_4\text{N}/\text{NG}$ indeed promotes the conversion to Li_2S as according to the order of $Q_{\text{low}}/Q_{\text{high}}$ showing as $\text{PP} < \text{NG} < \text{Co}_4\text{N}/\text{NG}$ (Figure 5F).

On the catalytic mechanism of Co_4N evolved in situ, we propose that CoS_x are the actual catalytic phases owing to the sharp comparison between $\text{Co}_4\text{N}_{(\text{pristine})}$ and $\text{Co}_4\text{N}_{(5\text{-cycle})}$. By correlating the catalytic activity of $\text{Co}_4\text{N}_{(\text{pristine})}$, $\text{Co}_4\text{N}_{(\text{ads})}$, and $\text{Co}_4\text{N}_{(5\text{-cycle})}$ to their sulfurization degree (that is, the number of inner CoS_x surface sites), we find that inner CoS_x should also account for polysulfide catalysis, indicating that a solid but labile catalyst such as $\text{Co}_4\text{N}/\text{CoS}_x$ undergoes dynamic recon-

struction to expose its internal interfaces to reactants and catalysis can take place at not only pristine solid surface but also internal mosaic interfaces. If the catalyst is initially inert, like Co_3O_4 , Co_9S_8 , and CoS_2 , sulfur can hardly penetrate in the bulk as deeply as in $\text{Co}_4\text{N}_{(5\text{-cycle})}$. Compared to ex situ synthetic CoS_x materials, in situ created CoS_x will have more opportunities to be exposed to polysulfides as these sites are naturally produced through polysulfide etching. More in-depth understanding into the catalytic and sulfurization mechanism requires precise tracking of phases and chemical states, for example, through isotope labeling. Nevertheless, the general concept can be easily applied to other metal-rich compounds such as $\text{Ni}_3\text{FeN}^{[18]}$ and Ni_3CoN (Supporting Information, Figures S32, S33).

Conclusion

We have unveiled the electrochemical phase evolution of (pre-)catalyst in aprotic and non-oxygen conditions, which renders a single-crystalline metal-rich compound suitable for interconnected ultrafine sulfide catalysts. Li-S batteries with Co_4N as the model pre-catalyst have achieved superior performance at kinetically harsh conditions such as at 10 C rate (16.7 mA cm^{-2}) and with a low E/S ratio of $4.7 \mu\text{L mg}_s^{-1}$. Our work will have wide implications for electrochemistry beyond Li-S batteries, such as other alkali metal (Li/Na/K)-chalcogen (S/O_2) batteries and materials beyond Co_4N , including the investigation of sulfides generated in situ as the true catalytically active phases, the design of novel electrocatalysts through electrochemical phase evolution, and the paradigm shift from aqueous to aprotic electrochemistry, which helps attain new understanding and new applications.

Acknowledgements

This work was supported by National Key Research and Development Program (2016YFA0202500, and 2016YFA0200102), National Natural Scientific Foundation of China (21776019 and 21825001), and Tsinghua University Initiative Scientific Research Program. The authors appreciate helpful discussion from Long Kong, Ze-Wen Zhang, and Ge Zhang.

Conflict of interest

The authors declare no conflict of interest.

Keywords: electrocatalysts · electrochemical phase evolution · lithium–sulfur batteries · polysulfide conversion

[1] I. L. C. Buurmans, B. M. Weckhuysen, *Nat. Chem.* **2012**, *4*, 873–886.

- [2] F. Tao, S. Dag, L. W. Wang, Z. Liu, D. R. Butcher, H. Bluhm, M. Salmeron, G. A. Somorjai, *Science* **2010**, *327*, 850–853.
- [3] M. W. Kanan, D. G. Nocera, *Science* **2008**, *321*, 1072–1075.
- [4] P. Z. Chen, K. Xu, Z. W. Fang, Y. Tong, J. C. Wu, X. L. Lu, X. Peng, H. Ding, C. Z. Wu, Y. Xie, *Angew. Chem. Int. Ed.* **2015**, *54*, 14710–14714; *Angew. Chem.* **2015**, *127*, 14923–14927.
- [5] L. A. Stern, L. G. Feng, F. Song, X. L. Hu, *Energy Environ. Sci.* **2015**, *8*, 2347–2351.
- [6] S. Jin, *ACS Energy Lett.* **2017**, *2*, 1937–1938.
- [7] P. G. Bruce, S. A. Freunberger, L. J. Hardwick, J. M. Tarascon, *Nat. Mater.* **2012**, *11*, 19–29; J. Lu, L. Li, J. B. Park, Y. K. Sun, F. Wu, K. Amine, *Chem. Rev.* **2014**, *114*, 5611–5640; Z. W. Seh, Y. M. Sun, Q. F. Zhang, Y. Cui, *Chem. Soc. Rev.* **2016**, *45*, 5605–5634.
- [8] A. Manthiram, Y. Z. Fu, S. H. Chung, C. X. Zu, Y. S. Su, *Chem. Rev.* **2014**, *114*, 11751–11787.
- [9] Y. X. Yin, S. Xin, Y. G. Guo, L. J. Wan, *Angew. Chem. Int. Ed.* **2013**, *52*, 13186–13200; *Angew. Chem.* **2013**, *125*, 13426–13441; D. Aurbach, B. D. McCloskey, L. F. Nazar, P. G. Bruce, *Nat. Energy* **2016**, *1*, 16128; Q. Pang, X. Liang, C. Y. Kwok, L. F. Nazar, *Nat. Energy* **2016**, *1*, 16132.
- [10] S. H. Oh, R. Black, E. Pomerantseva, J. H. Lee, L. F. Nazar, *Nat. Chem.* **2012**, *4*, 1004–1010; X. W. Gao, Y. H. Chen, L. R. Johnson, Z. P. Jovanov, P. G. Bruce, *Nat. Energy* **2017**, *2*, 17118; W. G. Lim, S. Kim, C. Jo, J. Lee, *Angew. Chem. Int. Ed.* **2019**, *58*, 18746–18757; *Angew. Chem.* **2019**, *131*, 18920–18931; H. Al Salem, G. Babu, C. V. Rao, L. M. R. Arava, *J. Am. Chem. Soc.* **2015**, *137*, 11542–11545; G. M. Zhou, H. Z. Tian, Y. Jin, X. Y. Tao, B. F. Liu, R. F. Zhang, Z. W. Seh, D. Zhuo, Y. Y. Liu, J. Sun, J. Zhao, C. X. Zu, D. S. Wu, Q. F. Zhang, Y. Cui, *Proc. Natl. Acad. Sci. USA* **2017**, *114*, 840–845; Z. H. Sun, J. Q. Zhang, L. C. Yin, G. J. Hu, R. P. Fang, H. M. Cheng, F. Li, *Nat. Commun.* **2017**, *8*, 14627; H. B. Lin, L. Q. Yang, X. Jiang, G. C. Li, T. R. Zhang, Q. F. Yao, G. W. Zheng, J. Y. Lee, *Energy Environ. Sci.* **2017**, *10*, 1476–1486; G. Li, X. L. Wang, M. H. Seo, M. Li, L. Ma, Y. F. Yuan, T. P. Wu, A. P. Yu, S. Wang, J. Lu, Z. W. Chen, *Nat. Commun.* **2018**, *9*, 705; J. R. He, G. Hartmann, M. Lee, G. S. Hwang, Y. F. Chen, A. Manthiram, *Energy Environ. Sci.* **2019**, *12*, 344–350; Z. Z. Du, X. J. Chen, W. Hu, C. H. Chuang, S. Xie, A. J. Hu, W. S. Yan, X. H. Kong, X. J. Wu, H. X. Ji, L. J. Wan, J. *Am. Chem. Soc.* **2019**, *141*, 3977–3985; J. Xie, B. Q. Li, H. J. Peng, Y. W. Song, M. Zhao, X. Chen, Q. Zhang, J. Q. Huang, *Adv. Mater.* **2019**, *31*, 1903813.
- [11] Z. W. Zhang, H. J. Peng, M. Zhao, J. Q. Huang, *Adv. Funct. Mater.* **2018**, *28*, 1707536.
- [12] H. D. Yuan, X. L. Chen, G. M. Zhou, W. K. Zhang, J. M. Luo, H. Huang, Y. P. Gan, C. Liang, Y. Xia, J. Zhang, J. G. Wang, X. Y. Tao, *ACS Energy Lett.* **2017**, *2*, 1711–1719; Y. R. Zhong, L. C. Yin, P. He, W. Liu, Z. S. Wu, H. L. Wang, *J. Am. Chem. Soc.* **2018**, *140*, 1455–1459.
- [13] D. R. Deng, F. Xue, Y. J. Jia, J. C. Ye, C. D. Bai, M. S. Zheng, Q. F. Dong, *ACS Nano* **2017**, *11*, 6031–6039.
- [14] Z. Yuan, H. J. Peng, T. Z. Hou, J. Q. Huang, C. M. Chen, D. W. Wang, X. B. Cheng, F. Wei, Q. Zhang, *Nano Lett.* **2016**, *16*, 519–527.
- [15] S. Feng, H. Zhong, J. H. Song, C. Z. Zhu, P. P. Dong, Q. R. Shi, D. Liu, J. C. Li, Y. C. Chang, S. P. Beckman, M. K. Song, D. Du, Y. H. Lin, *ACS Appl. Energy Mater.* **2018**, *1*, 7014–7021; H. Yuan, H. J. Peng, B. Q. Li, J. Xie, L. Kong, M. Zhao, X. Chen, J. Q. Huang, Q. Zhang, *Adv. Energy Mater.* **2019**, *9*, 1802768.
- [16] J. K. Nørskov, F. Studt, F. Abild-Pedersen, T. Bligaard, *Fundamental Concepts in Heterogeneous Catalysis*, Wiley, Hoboken, **2014**, pp. 1–96.
- [17] X. Liang, Y. Rangom, C. Y. Kwok, Q. Pang, L. F. Nazar, *Adv. Mater.* **2017**, *29*, 1603040; T. G. Jeong, D. S. Choi, H. Song, J. Choi, S. A. Park, S. H. Oh, H. Kim, Y. Jung, Y. T. Kim, *ACS Energy Lett.* **2017**, *2*, 327–333; Q. Pang, C. Y. Kwok, D. Kundu,

- X. Liang, L. F. Nazar, *Joule* **2019**, 3, 136–148; B. Y. Hao, H. Li, W. Lv, Y. B. Zhang, S. Z. Niu, Q. Qi, S. J. Xiao, J. Li, F. Y. Kang, Q. H. Yang, *Nano Energy* **2019**, 60, 305–311.
- [18] M. Zhao, H. J. Peng, Z. W. Zhang, B. Q. Li, X. Chen, J. Xie, X. Chen, J. Y. Wei, Q. Zhang, J. Q. Huang, *Angew. Chem. Int. Ed.* **2019**, 58, 3779–3783; *Angew. Chem.* **2019**, 131, 3819–3823.
- [19] G. Zhang, Z. W. Zhang, H. J. Peng, J. Q. Huang, Q. Zhang, *Small Methods* **2017**, 1, 1700134; B. Q. Li, H. J. Peng, X. Chen, S. Y. Zhang, J. Xie, C. X. Zhao, Q. Zhang, *CCS Chem.* **2019**, 1, 128–137.
- [20] F. Y. Fan, W. C. Carter, Y. M. Chiang, *Adv. Mater.* **2015**, 27, 5203–5209.
- [21] H. J. Peng, J. Q. Huang, X. Y. Liu, X. B. Cheng, W. T. Xu, C. Z. Zhao, F. Wei, Q. Zhang, *J. Am. Chem. Soc.* **2017**, 139, 8458–8466.
- [22] R. P. Fang, S. Y. Zhao, Z. H. Sun, W. Wang, H. M. Cheng, F. Li, *Adv. Mater.* **2017**, 29, 1606823; S. H. Chung, C. H. Chang, A. Manthiram, *Adv. Funct. Mater.* **2018**, 28, 1801188; Y. X. Yang, Y. R. Zhong, Q. W. Shi, Z. H. Wang, K. N. Sun, H. L. Wang, *Angew. Chem. Int. Ed.* **2018**, 57, 15549–15552; *Angew. Chem.* **2018**, 130, 15775–15778; M. Zhao, B. Q. Li, H. J. Peng, H. Yuan, J. Y. Wei, J. Q. Huang, *Angew. Chem. Int. Ed.* **2020**, <https://doi.org/10.1002/anie.201909339>; *Angew. Chem.* **2020**, <https://doi.org/10.1002/ange.201909339>.

Manuscript received: March 1, 2020

Accepted manuscript online: March 23, 2020

Version of record online: April 21, 2020